Journal of Materials Chemistry A

ROYAL SOCIETY OF CHEMISTRY

PAPER

View Article Online
View Journal

Cite this: DOI: 10.1039/d5ta06057e

Si-doped vanadium pentoxide/graphene xerogel nanocomposite cathodes with excellent cycle life for Li-ion batteries

Guangqi Zhu, †[a] Yadong Liu,†[a] Yikang Yu,[a] Mohammad Behzadnia,[a] Qi Zhang,[a] Chengjun Sun,[c] Yuzi Liu,[d] Yi-Kai Lien,[b] Wenquan Lu,[e] Mangilal Agarwal[fg] and Jian Xie *[ab]

Vanadium pentoxide (V_2O_5) is a promising cathode material for lithium-ion batteries due to its high theoretical specific capacity (443 mA h g^{-1}) and specific energy (1218 Wh kg^{-1} at 2.75 V). However, its large-scale application is limited by its poor electrical conductivity and structural instability, leading to irreversible capacity loss, consequently, short cycle life, and low-rate capability. In this work, we developed a 3D nanostructured xerogel composite by uniformly doping silicon (Si) into the V_2O_5 framework, which anchors on the surface of graphene sheets *via* a sol–gel process. The optimized Si-doped V_2O_5 on the graphene (Si-V_2O_5@G) composite, containing 10 wt% Si and 2 wt% graphene, delivers a high specific capacity of 392 mA h g^{-1} at 0.1C rate and excellent cycling stability: 589 cycles with 80% capacity retention at a high rate of 1.0C, and a very low capacity fading rate of 0.03% capacity loss per cycle—significantly surpassing the best performance of up-to-date V_2O_5 work (*e.g.* the best performance of 160 mA h g^{-1} and 300 cycles at 0.75C rate and 0.13% capacity loss per cycle). Scanning Transmission Electron Microscopy (STEM) reveals uniform Si distribution, which leads to much larger V_2O_5 nanoribbons over the graphene sheets (observed using TEM). Such a nanocomposite structure is capable of tolerating more structural change during the (de) lithiation process, resulting in a much improved cycle life. Electrochemical impedance spectroscopy (EIS) and cyclic voltammetry (CV) further demonstrate the improved conductivity and structural integrity. X-ray photoelectron Spectroscopy (XPS) manifests the interaction of doped Si with the V–O system. The *in operando* XANES and EXAFS analyses suggest the increased multi-valence change among V^{5+}, V^{4+}, and V^{3+} states in the (de)lithiation process after Si-doping. Additionally, EXAFS analysis indicates that Si doping effectively stabilizes the local V–O coordination environment, facilitating better Li^+ insertion/extraction reversibility and reducing the degradation of Si-V_2O_5@G systems. This work demonstrates a cost-effective, non-metal doping strategy for enhancing the electrochemical performance of high-energy-density metal oxide cathodes for next-generation LIBs.

Received 27th July 2025
Accepted 6th February 2026

DOI: 10.1039/d5ta06057e

rsc.li/materials-a

1. Introduction

Lithium-ion batteries (LIBs) have become indispensable energy storage devices in many applications in today's society, ranging from portable electronics to electric vehicles,[1–7] driving the demand for higher energy density to meet the increasing needs of the energy storage market. However, conventional intercalation-type cathode materials such as $LiFePO_4$ and $LiCoO_2$ are limited by a one-electron transfer mechanism, limiting their theoretical capacities and impeding further improvements in energy density.[8–12] Among alternative high-capacity cathode candidates, vanadium pentoxide (V_2O_5) has drawn considerable attention due to its low cost, natural abundance, and a high theoretical capacity of 443 mA h g^{-1}, stemming from its ability to intercalate up to three lithium ions per formula unit over a broad voltage window (1.5–4.0 V *vs.* Li^+/Li).[13–21] Despite these advantages, practical implementation of V_2O_5 as commercial cathodes is hampered by

[a]*School of Mechanical Engineering, Purdue University, West Lafayette, Indiana 47906, USA. E-mail: jxie@purdue.edu*

[b]*School of Materials Engineering, Purdue University, West Lafayette, Indiana 47906, USA*

[c]*Advanced Photon Source, Argonne National Laboratory, 9700 South Cass Avenue, Lemont, Illinois 60439, USA*

[d]*Center for Nanoscale Materials, Argonne National Laboratory, 9700 South Cass Avenue, Lemont, Illinois 60439, USA*

[e]*Chemical Science and Engineering Division, Argonne National Laboratory, 9700 South Cass Avenue, Lemont, Illinois 60439, USA*

[f]*Department of Biomedical Engineering, Indiana University Indianapolis, Indianapolis, Indiana 46202, USA*

[g]*Integrated Nanosystems Development Institute, Indiana University Indianapolis, Indianapolis, Indiana 46202, USA*

† Contribute equally to this work.

severe structural evolution and rapid capacity fading during deep (de)lithiation, especially when engaging the full three-electron redox process.[22] These challenges arise from phase transitions involving crystalline and amorphous states (*e.g.*, ω-$Li_xV_2O_5$ to β-$Li_{0.3}V_2O_5$)[14,23–25] and significant short-range order (SRO) evolution that destabilizes the electrode materials. Recent advances in cation-disordered rock-salt-type cathode materials suggest that the heterogeneous element doping effect can suppress detrimental SRO evolution and enhance structural resilience.[11,19,20,22,25,26] Multiple doping of heteroatoms into a material can result in the increased thermodynamic intrinsic stability, which has been demonstrated in recent high entropy catalysts[27] and battery electrode materials.[18,28] In our previous work, we took the approach of using the graphene sheet to (1) improve the local electronic conduction on the nanoscale and (2) stabilize the V_2O_5 structure by sandwiching V_2O_5 nanoribbons between two graphene sheets to maintain the structural integrity during (de)lithiation.[29,30] Such an approach achieved theoretical specific capacity and 120 cycles with 80% initial capacity.[31]

A cost-effective, nonmetal entropy-engineering strategy by introducing silicon (Si), the second most abundant element on Earth's crust, into the V_2O_5 lattice and incorporating graphene to form a robust 3D nanostructure *via* a sol–gel process has been developed in the past work.[9,17,26,32,33] Based on this concept, we developed a Si-doped V_2O_5/graphene composite (Si-V_2O_5@G) cathode herein to achieve uniform Si distribution and enhanced structural stability. Electrochemical testing demonstrates the outstanding performance, with the optimized Si-V_2O_5@G (10 wt% Si, 2 wt% graphene) delivering a high specific capacity of 392 mA h g^{-1} at 0.1C and achieving 589 cycles at a fairly high 1C rate with 80% of its initial capacity and a very low capacity fading rate of 0.03% capacity loss per cycle—significantly surpassing the performance of most of the V_2O_5 work (*e.g.* the best performance of 160 mA h g^{-1} and 300 cycles at 0.75C rate and 0.13% capacity loss per cycle[26]) reported up to now (Table S1). STEM manifested that Si doping could lead to much larger V_2O_5 nanoribbons over the graphene sheets, which can tolerate more structural change during the (de)lithiation process, resulting in a much improved cycle life. Cyclic voltammetry and impedance spectroscopy confirm that Si doping enhances electronic conductivity and reduces charge transfer resistance. The XPS analysis displays the doping effect of Si on the V_2O_5 structures, which indicates strong binding effects of Si–O–V. Moreover, *in operando* XANES and EXAFS analyses[34] reveal that Si doping stabilizes the V–O framework and promotes reversible valence-state transitions of vanadium, enabling a complete and symmetric (de)lithiation process. These results underscore the efficacy of Si doping simultaneously enhancing both structural and electrochemical stability, offering a promising pathway for the development of next-generation high-energy cathode materials.[35–41]

2. Experimental methods

2.1 Materials

$LiPF_6$ (battery grade), ethylene carbonate (EC) and ethyl carbonate (EMC) were obtained from Novolyte Technologies (Independence, OH, USA) for electrolyte preparation. $NaVO_3$ (99.5%) and Na_2SiO_3 (99%) were purchased from Sigma-Aldrich. Proton-exchange resin (Dowex-50-WX2) with 50–100 mesh was obtained from Thermo Scientific Chemicals. Super P conductive carbon black was purchased from MTI Corporation (Richmond, CA, USA) and used without further treatment.

2.2 Synthesis of a Si-doped V_2O_5 xerogel

The V_2O_5 xerogel was synthesized using our previous modified ion exchange method.[42,43] Around 100 mL of 0.1 M $NaVO_3$ aqueous solution was eluted through a column loaded with a proton exchange resin. The obtained yellow solution of HVO_3 was aged in a glass container for 3 weeks to obtain a mature homogeneous V_2O_5 hydrogel. The dried V_2O_5 xerogel was obtained by freeze-drying the above hydrogel under vacuum for about a week. The Si-doped V_2O_5 xerogel was prepared by additionally mixing Na_2SiO_3 into the 0.1 M $NaVO_3$ solution and following the same procedures as for the preparation of the V_2O_5 xerogel.[15,16,44]

2.3 Synthesis of GO

Graphene oxide was prepared based on our previous method[42,43] and more details can be found in the SI. The synthesized GO was dispersed in purified deionized (DI) water with a concentration of about 10 mg mL^{-1}.[17,31]

2.4 Synthesis of V_2O_5@G and Si-V_2O_5@G

The V_2O_5@G hybrid was prepared by mixing the prepared GO suspension and the yellow solution of HVO_3 generated by proton exchange at the desired ratio. The obtained dark yellow solution was aged in a glass container for 3 weeks to obtain a completely cured, homogeneous V_2O_5/GO hydrogel. The dried V_2O_5@GO xerogel was obtained by freeze-drying the V_2O_5@GO hydrogel under vacuum in a freeze-dryer. The formed V_2O_5@GO xerogel was heated and annealed in an inert environment (N_2) at a rate of 5 °C min^{-1} up to 400 °C and kept at 400 °C for 6 h, during which the GO was reduced to graphene and the graphene-modified V_2O_5 hybrid (V_2O_5@G) was formed. The graphene-modified Si-doped V_2O_5 hybrid (Si-V_2O_5@G) was prepared by mixing the GO suspension with the solution of HVO_3 and H_2SiO_3 generated by proton exchange and following the same procedures as for the V_2O_5@G preparation. For comparison, additional two samples, V_2O_5 and Si doped V_2O_5 (Si-V_2O_5), were prepared without mixing with the GO suspension and then underwent the same treatment as V_2O_5@G and Si-V_2O_5@G. The mass percentage of vanadium in V_2O_5, V_2O_5@G, Si-V_2O_5 and Si-V_2O_5@G is 56.0 wt%, 54.9 wt%, 49.4 wt% and 49.2 wt%, respectively.

2.5 Electrochemical characterization

The electrodes were prepared by casting a slurry of 80 wt% active materials (V_2O_5@G and Si-V_2O_5@G, respectively), 10 wt% polyvinylidene difluoride (PVDF), and 10 wt% Super P onto a 10 μm-thick sheet of Al foil. For comparison, the electrodes of V_2O_5 and Si-V_2O_5, which were synthesized using the same methods except for the addition of GO, were prepared. The prepared electrodes were placed in a vacuum oven and allowed to dry at 90 °C for 24 h. The electrolyte consisted of 1.2 M $LiPF_6$ in a mixture of

ethylene carbonate (EC) and ethyl-methylene carbonate (EMC) solvent (3:7, by weight). The prepared electrodes were assembled into 2016-type coin cells using Li metal anodes (Aldrich, USA) and Celgard 2400 separators (Celgard, Ohio, USA) to characterize their electrochemical performance. These cells were tested using an Arbin battery cycler (BT-2000, Arbin, TX, USA) with different C-rates between 1.5 and 4.0 V. A Solartron 1287A/1260A Potentiostat/Impedance System (Solartron Analytical, England, UK) was used to measure the AC impedance of these cells in the frequency range of 0.01 Hz–1 MHz with a voltage amplitude of 5 mV. The results were fitted using the equivalent circuit, where R_0 is the contact resistance, R_e and C_e refer to the resistance and capacitance of the V_2O_5 electrode, R_{ct} and C_{dl} stand for the charge-transfer resistance of the redox reaction of vanadium in V_2O_5 and the double-layer capacitance in the electrode, respectively, and W_d refers to the Warburg diffusion impedance, which could reflect the diffusion of Li ions in V_2O_5.

2.6 Materials characterization

Scanning electron microscopy (SEM) and energy-dispersive X-ray spectroscopy (EDXS) were conducted using a JEOL 7800 SEM (Japan) operating at 5 kV. High-resolution transmission electron microscopy (HRTEM) was performed on a FEI Talos microscope (USA) operated at 80 kV. Synchrotron radiation-based *in operando* X-ray absorption spectroscopy (XAS) was employed to investigate the dynamic electrochemical behavior of the V_2O_5 cathodes. X-ray photoelectron spectroscopy (XPS) was performed using a PHI 5000 VersaProbe II system attached to an Ar-filled glovebox with monochromatic Al Kα radiation. X-ray powder diffraction (XRD) was conducted using Bruker D8 Discover, Bruker USA. In particular, *in operando* X-ray absorption near-edge structure (XANES) spectroscopy was used to probe the oxidation state and local structural changes of vanadium across all phases during cycling. *In operando* XANES measurements were carried out on the coin cells incorporating V_2O_5@G and Si-V_2O_5@G electrodes at beamline 20-BM-B of the Advanced Photon Source (APS), Argonne National Laboratory. Coin cells with 2 mm diameter holes at the center were prepared for the *in operando* study, sealed with Kapton tape to allow X-ray penetration while maintaining an inert environment. The vanadium K-edge (5463.76 eV) was monitored in transmission mode using a Si (111) monochromator. Energy calibration was performed using the first derivative of the vanadium metal reference spectrum, which was simultaneously collected in a dedicated reference channel for each measurement. Identical electrodes were used in all cells to ensure consistency and improve signal-to-noise ratios. Electrochemical cycling was conducted at a constant current of ~0.5C between 1.7 V and 3.6 V. XANES data processing and analysis were performed using the ATHENA software package following standard protocols.

3. Results and discussion

3.1 Synthesis and morphology of Si-doped V_2O_5 on graphene

The graphene supported Si-doped V_2O_5 (Si-V_2O_5@G) was synthesized *via* a modified ionic exchange method.[31] As shown in Fig. 1a, a well-mixed aqueous solution of $NaVO_3$ and Na_2SiO_3 was eluted through an ion exchange/separation column filled with proton exchange resin. During the process, the sodium ions were exchanged with protons (H^+) and immobilized in the resin, while VO_3^- and SiO_3^{2-} further acquired a proton and became HVO_3 and H_2SiO_3 in the resulting solution, followed by uniform mixing with GO suspension. An olation reaction along the H_2O–V–OH direction to expand the coordination of vanadium, incorporated with Si, occurred during the subsequent aging procedure, during which the resulting solution turned dark red with increasing viscosity. Finally, V_2O_5@G was obtained after freeze drying and annealing processes. The SEM image of Si-V_2O_5@G is shown in Fig. 1b, in which a sheet stacked morphology of Si-V_2O_5 sheets supported on the planar graphene surface. The corresponding EDXS mapping (Fig. 1c–e) shows that V and Si are uniformly distributed over the surface of sheets, which indicates that Si has been uniformly doped into the V_2O_5 structure. The EDXS mapping also demonstrates the uniform distribution of carbon, indicating the distribution of V_2O_5 on graphene sheets.[17] The TEM analysis in Fig. 1f shows that Si-V_2O_5@G displays the nanoribbon-like structure supported on the graphene sheet. The average diameter of the Si-V_2O_5 nanoribbons is 100 nm with an outstanding morphology, as shown in Fig. 1g. The corresponding selected area electron diffraction (SAED) (Fig. 1h) on the single nanoribbon in Fig. 1f shows the lattice structure corresponding to the (010), (100) and (110) crystal planes of V_2O_5, while no SiO_2 lattice was detected, indicating the successful doping of Si into the V_2O_5 structure instead of the formation of a SiO_2 phase. The above phenomenon is also consistent with the XRD results (Fig. S2), where no SiO_2 phase was detected in both Si-V_2O_5 and Si-V_2O_5@G systems. Compared with Si-V_2O_5@G, the V_2O_5@G without Si doping reveals much smaller sized nanoribbons, with an average diameter of 50 nm, as shown in Fig. 1i. The comparatively larger size of nanoribbons in Si-V_2O_5@G suggests that the doping of Si into the V_2O_5 lattice can increase the crystal size of the structure, making it more robust during the (de)lithiation process, resulting in a significantly improved cycle life. The STEM EDXS mapping of V_2O_5@G (Fig. S1) manifests the uniform distribution of V, O and C, suggesting the outstanding formation of the V_2O_5 structure sitting on a graphene sheet. The STEM EDXS mapping of Si-V_2O_5@G (Fig. 1j–n) further demonstrates the uniform distribution of Si, V and O within the Si-V_2O_5 nanostructure, indicating the excellent doping of Si into the V_2O_5 structure at the nanocrystalline scale. The XRD analysis exhibits that both V_2O_5@G and Si-V_2O_5@G are non-crystalline structures when integrated with the graphene matrix, while pure V_2O_5 and Si-V_2O_5 display a crystalline structure after thermal treatment at 400 °C. Besides, the XRD analysis of Si-V_2O_5@G shows that Si doping introduces more peaks around the smaller 2-theta region compared with Si-V_2O_5@G, which may result in the larger nanoribbons.

3.2 Electrochemical performance and stability

To evaluate the electrochemical performance and cycling stability of the Si-V_2O_5@G materials, coin-type cells were

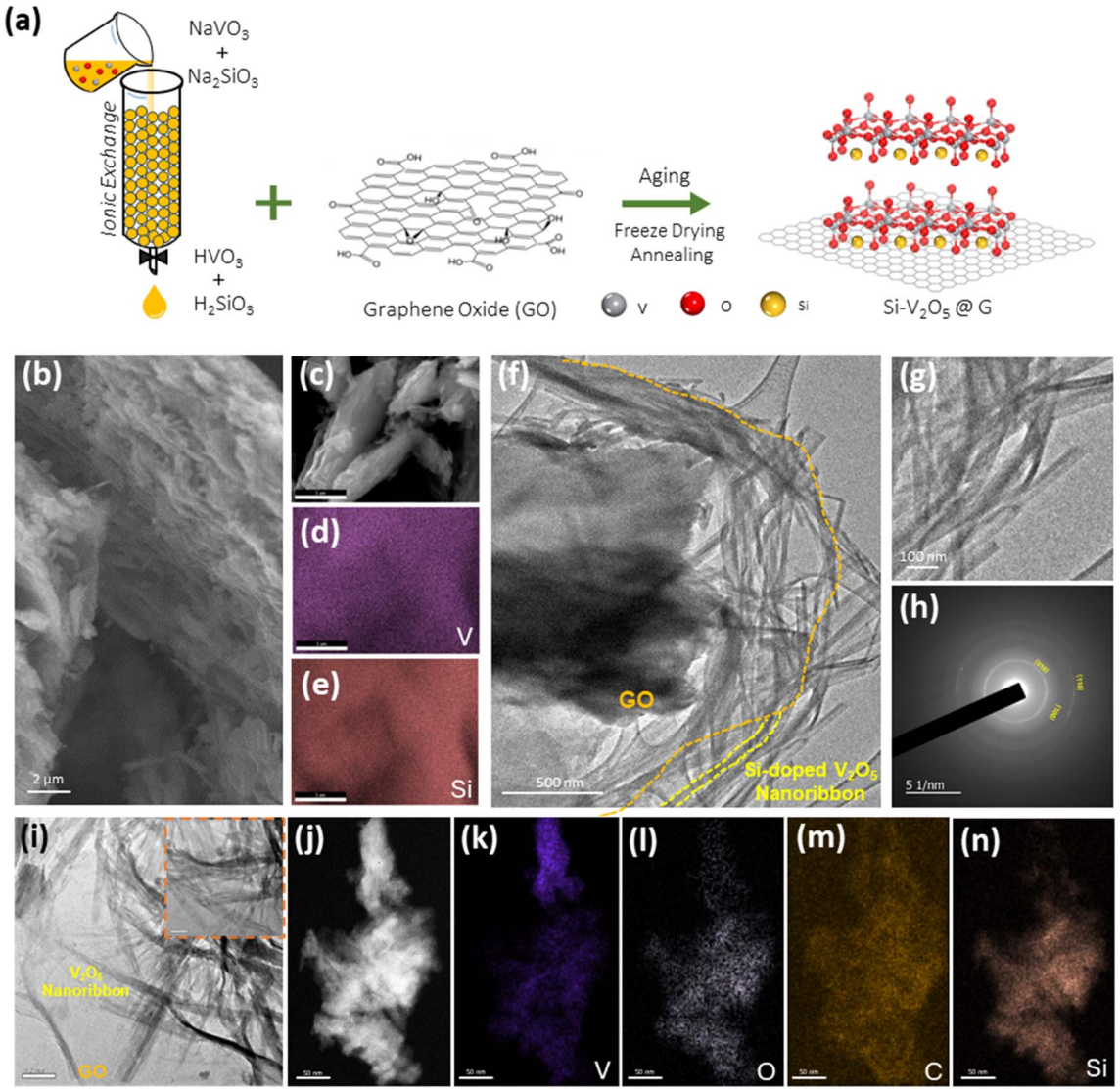

Fig. 1 Synthesis schematic and morphology analysis. (a) Schematically illustrated synthesis of the self-assembled Si-V_2O_5@G sample. (b) SEM images and (c–e) corresponding EDXS analysis. (f) TEM images of Si-V_2O_5@G, (g) high-resolution TEM image and (h) corresponding SAED pattern. (i) TEM images of pure V_2O_5/G. (j–n) TEM EDXS analysis of the Si-V_2O_5@G sample.

assembled with Li metal as the counter and reference electrode. The cycling stability was evaluated based on galvanostatic charge–discharge at 1.0C. As shown in Fig. 2a, Si-V_2O_5@G demonstrates significantly improved stability and achieved 589 cycles at a fairly high 1C rate with 80% of its initial capacity with a very low capacity fading rate of 0.03% capacity loss per cycle—significantly surpassing the performance of most V_2O_5 cathodes (*e.g.* the best performance of 160 mA h g^{-1} and 300 cycles at 0.75C rate with 0.13% capacity loss per cycle[26]) reported up to now (Table S1). This improvement is much better than that of V_2O_5@G (102 cycles with 80% capacity retention). In addition, it was found that the cycling stability of both V_2O_5@G and Si-V_2O_5@G is higher than that of pure V_2O_5 and Si-V_2O_5, which indicates that the incorporation of graphene sheets can also improve the stability of the V_2O_5 nanoribbons. Such an improvement from the graphene sheets can be attributed to the greatly enhanced electric conduction between V_2O_5 units within the V_2O_5 nanoribbons while the graphene sheet provides an electron transport path and enhances the structural integrity of V_2O_5 nanoribbons by sandwiching them between two neighboring graphene sheets. Moreover, for both V_2O_5 cathodes with or without incorporation of graphene, the addition of Si doping can significantly improve stability. The enhanced stability should originate from the doping of Si into the V_2O_5 nanostructure, possibly the larger sized V_2O_5 nanoribbons, and thus improving the structural stability and reversibility. Furthermore, the rate performance of these cathode materials was recorded at various current densities and is illustrated in Fig. 2b. Both Si-V_2O_5@G and V_2O_5@G have the same rate capability until 1C rate while V_2O_5@G has increasingly improved rate capability as the rate is beyond 1C. This also supports the hypothesis that doping Si leads to larger sized V_2O_5

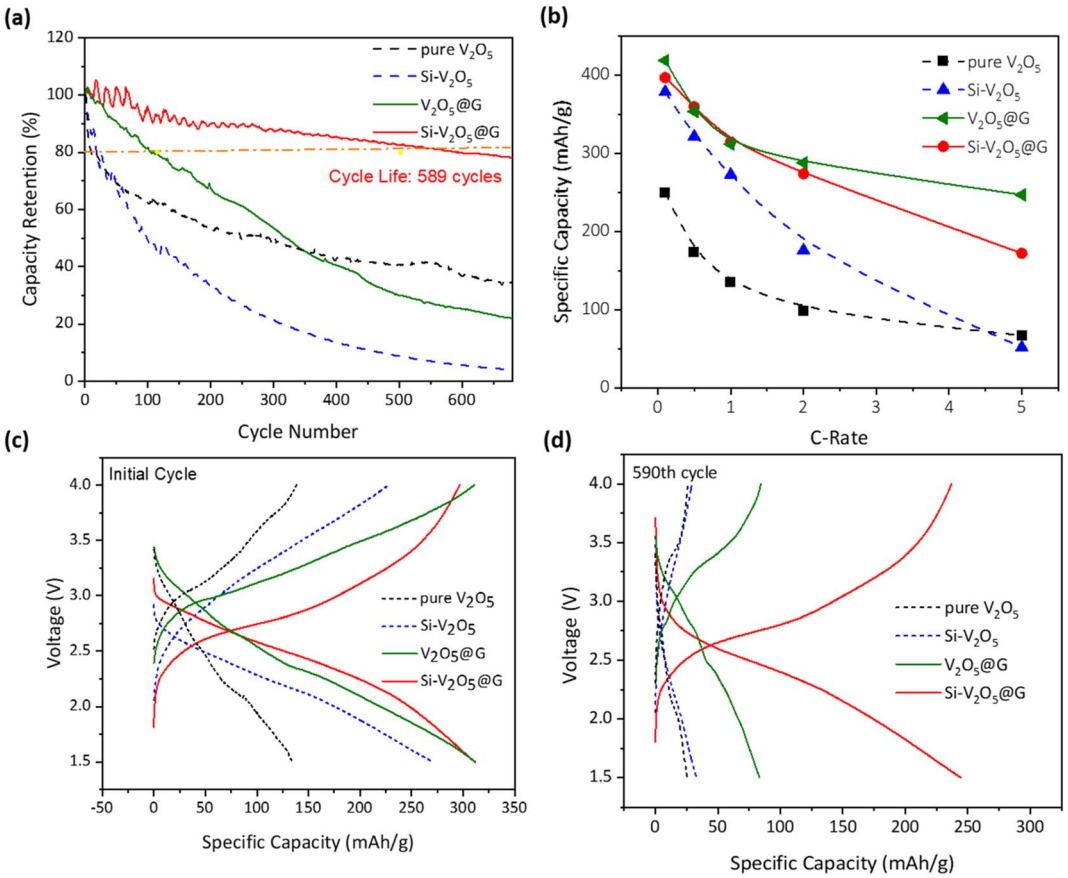

Fig. 2 Electrochemical performance of different V_2O_5 cathodes; electrolyte: 1.2 M $LiPF_6$ in EC : EMC (3 : 7 by weight), 2016-type coin cell, anode: Li metal, separator: Celgard 2400, and room temperature. (a) Capacity retention cycled at 1.0C. (b) Rate capability performance. (c) Initial discharge and charge curve at 1.0C rate. (d) The end-of-life discharge and charge curve at 1.0C rate.

nanoribbons, which are responsible for improved stability. The larger V_2O_5 nanoribbons help tolerate more lattice strain change during (de)lithiation, maintain the structural integrity and enable higher cycle life. On the other hand, the graphene sheet can improve the electronic conductivity between the V_2O_5 units (*i.e.* bipyramids) of the V_2O_5 nanoribbon, while the graphene sheet cannot enhance the electronic conductivity within the V_2O_5 nanoribbon. Larger-sized ribbons may result in lower electronic conduction within the V_2O_5 nanoribbon due to the elongated electron transport length. Besides, the non-crystalline structure (*i.e.* amorphous) of Si-V_2O_5@G and V_2O_5@G, which is displayed in XRD (Fig. S2), provides much more configurational stability during cycling compared with pure V_2O_5 and Si-V_2O_5 with much more crystalline structures. The corresponding specific capacity of Si-V_2O_5@G is 397, 360, 315, 274 and 172 mA h g^{-1}, similar to that of V_2O_5@G (419, 354, 312, 288, and 247 mA h g^{-1}, respectively) at the current densities of 0.1, 0.5, 1.0, 2.0 and 5.0C. In addition, compared with Si-V_2O_5, Si-V_2O_5@G exhibits significantly higher specific capacity, especially at larger current densities, which suggests that the incorporation of graphene can effectively increase the large-current capacity due to the improved conductivity. From our previous work,[42] the initial cycle of charge and discharge curves of pristine V_2O_5 displays three plateaus, which corresponds to the crystalline-to-crystalline transitions with a sequence of α-$Li_xV_2O_5$, ε-$Li_xV_2O_5$, δ-$Li_xV_2O_5$, γ-$Li_xV_2O_5$, and ω-$Li_xV_2O_5$. While for V_2O_5@G, Si-V_2O_5, and Si-V_2O_5@G in Fig. 2c, no plateaus were observed in the initial discharge process, which indicates the non-crystalline properties compared with pristine V_2O_5.[23,44–47] The non-crystalline (*i.e.* amorphous) V_2O_5 has higher cycling stability compared with crystalline V_2O_5 due to its reversible structural change. Furthermore, there are much smaller differences for the charge and discharge curves between the initial and final (590th) cycles for Si-V_2O_5@G compared with V_2O_5 (Fig. 2d), which demonstrates the outstanding cycling stability of Si-V_2O_5@G and shows much better performance compared with the other samples. Besides, Si-V_2O_5@G also displays outstanding and improved stability compared with other recent published studies (Table S1). Overall, the introduction of Si leads to large V_2O_5 nanoribbons, which change the V_2O_5 long-term structure from crystalline to non-crystalline and significantly improves the cycling stability.

3.3 EIS, CV curves and XPS analysis on Si doping

To investigate the cause of the significantly improved cycling stability, the electrochemical processes upon lithium insertion and extraction were studied using electrochemical impedance

spectroscopy (EIS) and cyclic voltammetry (CV), as shown in Fig. 3. The CV curves show the positions of different redox peaks for the reversible reactions between different valence states of vanadium. As shown in Fig. 3a, broader peaks were found in the CV curves of Si-V_2O_5@G, which correspond to the initial charge and discharge processes. A large oxidation peak was seen around 3.25 V after a shallow oxidation peak around 2.25 V, while reduction peaks at 2.6 V and 1.7 V were observed, respectively, for the 1st CV cycle of Si-V_2O_5. In the following cycles, only two major peaks appear: an oxidation peak at 3.80 V and a reduction peak at 1.75 V, corresponding to the oxidation state change of vanadium. Compared with Si-V_2O_5, Si-V_2O_5@G shows an oxidation peak at 3.3 V and a reduction peak at 2.4 V for the 1st cycle with reduction peak shifting toward 2.3 V for the 3rd cycle. Si-V_2O_5@G demonstrates much better cycling stability with each cycle as the CV curves keep the same shape and peaks, similar to those in the first cycles. To better understand the effects of Si doping in V_2O_5 on the cycling stability and electrochemical behaviors, the EIS analysis was conducted. The Nyquist plots of pure V_2O_5, V_2O_5@G, Si-V_2O_5@G and Si-V_2O_5@G after initial 3 cycles at a current density of 0.1C are shown in Fig. 3b, along with the corresponding equivalent electrical circuit for fitting. The total impedance was divided into four components, the contact resistance R_0, the electrode resistance R_e, the charge-transfer resistance R_{ct} and the Warburg diffusion impedance W_d. The diameter of the semicircle in the high frequency range represents the charge transfer resistance, R_{ct}, including the resistance of desolvation of the solvated Li ions in the electrolyte, Li-ion transport in the solid electrolyte interphase or cathode–electrolyte interphase layer, and the final acceptance of electrons in the host structures. Therefore, charge transfer resistance is significantly relevant to lithium insertion and extraction kinetics. As shown in Fig. 3a, the charge transfer resistance of Si-V_2O_5 decreases obviously from 46.9 Ω of pristine V_2O_5 to 28.2 Ω, and that of Si-V_2O_5@G decreases from 10.9 Ω of V_2O_5@G to 9.8 Ω, which indicates that the introduction of Si promotes the lithium reaction kinetics. In addition, both V_2O_5@G and Si-V_2O_5@G show smaller charge transfer resistance, which corresponds to the improved electron transport between V_2O_5 bi-pyramid units.

The XPS analysis (Fig. 3c–f) was performed to investigate the electronic structures and valence-state evolution of vanadium in the V_2O_5 structures as a function of Si doping and graphene incorporation. Fig. 3c and d present the high-resolution V_{2p} spectra of Si-V_2O_5@G and V_2O_5@G, respectively. For pristine V_2O_5@G, the $V_{2p3/2}$ peak is centered at 517.18 eV, which represents the state of V^{5+} in V_2O_5. Upon Si doping, this peak shifts remarkably to a lower binding energy of 516.35 eV in Si-V_2O_5@G. This significant negative shift indicates an increased electron density around the vanadium centers, suggesting a partial reduction of V^{5+} to V^{4+} species. The observed binding-energy shift can be attributed to electronic interactions induced by Si incorporation into the V_2O_5 lattice, where Si acts as an electron donor and modifies the local coordination environment of vanadium. Such an electronic redistribution facilitates charge transfer toward the V–O framework, leading to a lowered average oxidation state of vanadium. This effect is further stabilized by the graphene support, which enhances interfacial charge delocalization and suppresses electron localization.

Additionally, more evidence for successful Si incorporation is provided by the Si_{2p} XPS spectrum (Fig. 3g and h), which reveals a dominant Si–O bonding feature, confirming that Si is chemically integrated into the oxide framework rather than existing as a separate phase, such as SiO_2. Notably, the Si–O peak exhibits a slight binding-energy shift compared to crystalline SiO_2, which can be attributed to the distorted and partially amorphous local environment arising from graphene incorporation. This shift strongly suggests the formation of interfacial Si–O–V bonds within the Si-V_2O_5@G structure, further corroborating lattice-level doping rather than surface adsorption of Si. The XPS results demonstrate that Si doping effectively tailors the electronic structure of V_2O_5 by inducing partial vanadium reduction and strengthening interfacial bonding, which plays a significant role in enhancing the electrochemical stability and activity of the Si-V_2O_5@G nanostructure.

3.4 *In operando* XANES and EXAFS analysis

In operando X-ray absorption near-edge structure (XANES) spectroscopy was employed to investigate the (de)lithiation mechanism of V_2O_5-based cathodes by monitoring the changes in the electronic structure during electrochemical cycling.[13,35,48] Specifically, the evolution of the vanadium oxidation state was tracked during the charge and discharge processes, offering a critical insight into the structural reversibility of the V_2O_5-based cathodes. The binding energy shift observed in XANES spectra serves as a direct reflection of changes in the vanadium valence states and thus can be effectively used to evaluate the reversibility and stability of the cathode material structure. The comparative *in operando* XANES spectra of blank Li/V_2O_5@G and Li/Si-V_2O_5@G coin cells during the first and second discharge/charge cycles are presented in Fig. 4a. For both V_2O_5@G and Si-V_2O_5@G, the energy shifts (contour plots Fig. 4a and b) observed during lithiation and delithiation were largely symmetric, suggesting the good structural reversibility in both systems. However, the degree of the energy shift and the shape of the spectra are significantly different. Pristine V_2O_5@G exhibits more pronounced changes in its XANES spectra across both cycles compared to the Si-doped variant. These more substantial shifts suggest that the undoped V_2O_5 structure undergoes more significant electronic and structural fluctuations during cycling, which indicates greater instability and irreversibility. In contrast, the smaller energy shifts and smoother spectral evolution observed in Si-V_2O_5@G indicate a more stable electronic structure and enhanced structural robustness during lithium insertion and extraction. Fig. 4c and d display typical K-edge XANES spectra of the two cathodes during the first discharge process. V_2O_5@G exhibits substantial shifts in the absorption edge, indicating the notable changes in the oxidation state and coordination environment of vanadium during lithiation. This large shift implies a significant alteration in the electronic structure, which can be associated with more severe lattice distortion and lower cycling stability. In contrast,

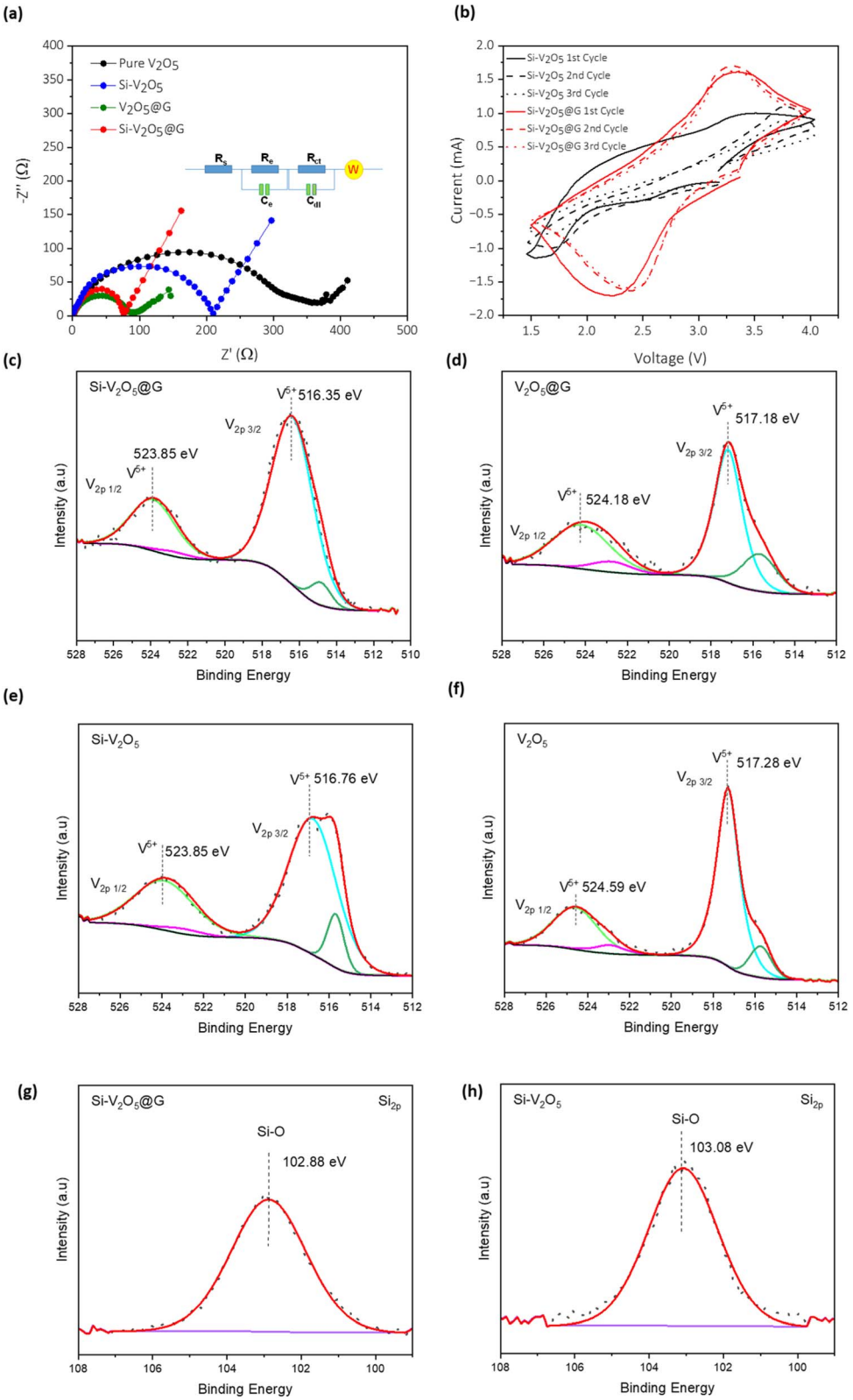

Fig. 3 (a) Voltammetry cycling analysis of Si-V_2O_5-based materials. (b) Electrochemical impedance spectroscopy (Nyquist plot) of Si-V_2O_5-based materials. (c–h) XPS analysis of V_{2p} and Si_{2p} of V_2O_5-based materials.

Si-V_2O_5@G showed moderate shifts in the absorption edge, implying less drastic changes in the local electronic structure and suggesting a more stable lithiation process, which is in consistent with the XPS analysis. Additionally, the Si-doped V_2O_5 demonstrates more symmetric spectral changes during charging and discharging compared to pristine V_2O_5,

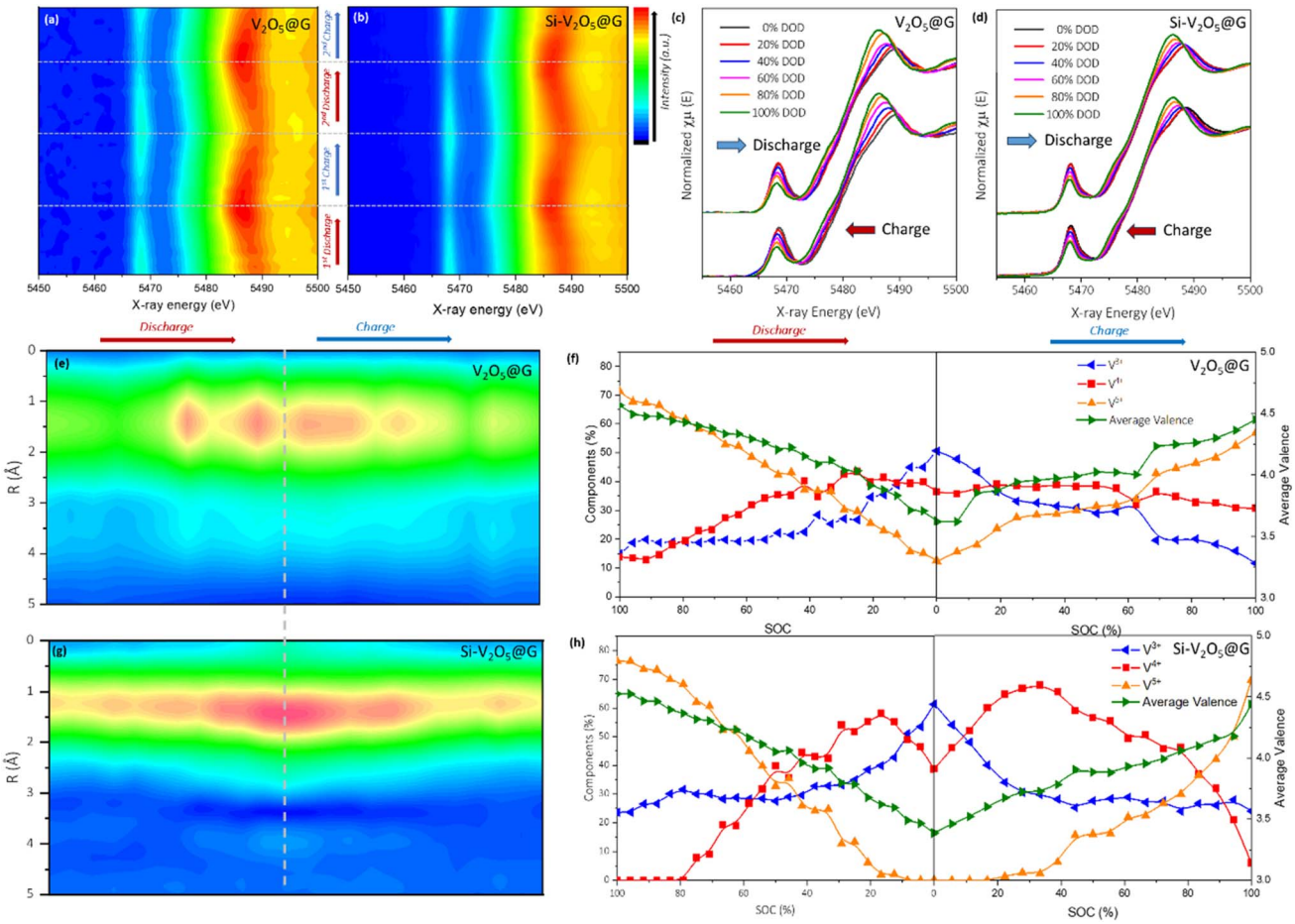

Fig. 4 *In operando* X-ray Absorption Spectroscopy (XAS) characterization. Normalized X-ray Absorption Near Edge Spectroscopy (XANES) 2D contour plots of (a) Li/V_2O_5@G and (b) Li/Si- V_2O_5@G coin cells during 1st and 2nd discharge/charge cycling. Typical K-edge XANES spectra of (c) Li/V_2O_5@G and (d) Li/Si-V_2O_5@G coin cells during the first discharge/charge process. EXAFS 2D contour plots of (e) Li/V_2O_5@G and (g) Li/Si-V_2O_5@G coin cells during 1st discharge/charge cycling. Valence fitting results of the first discharge/charge process of (f) pristine V_2O_5@G and (h) Si-V_2O_5@G.

reinforcing the notion that Si doping contributes to improved structural reversibility and cycling stability.[49–52]

To further explore the local structural environment of vanadium in these two systems, extended X-ray absorption fine structure (EXAFS) analysis was performed during the initial lithiation and delithiation cycles. The EXAFS spectra provide detailed information about the short-range ordering and local atomic interactions, particularly the V–O–Li coordination that forms during lithium insertion. Fig. 4e presents the EXAFS 2D contour plots for V_2O_5@G during the initial charge/discharge process. A prominent peak at approximately 1.3 Å was observed, corresponding to the V–O–Li interaction. As the state of charge (SOC) increases, the intensity of this peak gradually rises, reflecting the enhanced V–O–Li interaction due to the progressive intercalation of Li^+ ions into the V_2O_5 lattice. However, during the delithiation process, the peak intensity did not fully return to its original state, indicating incomplete recovery of the V–O coordination environment. This asymmetry in the EXAFS intensity between discharge and charge cycles strongly suggests that the V_2O_5 structure is not fully reversible after a complete lithiation–delithiation cycle. The inability to fully extract Li^+ ions from the V_2O_5 structure and restore the original lattice contributes to long-term capacity fading and performance degradation. In contrast, Si-V_2O_5@G shows a highly reversible pattern in the EXAFS 2D contour plot in Fig. 4g under the same cycling conditions. Similar to the pristine sample, a V–O–Li peak at ~1.3 Å was observed, and its intensity increased with SOC. However, unlike V_2O_5@G, the peak intensity in the Si-doped system returned to nearly its original state after delithiation. This symmetric behavior in EXAFS intensity suggests that the V–O–Li coordination in Si-V_2O_5@G is more reversible, implying improved structural integrity during cycling. The data provide strong evidence that Si doping effectively stabilizes the local V–O coordination environment, facilitating better Li^+ insertion/extraction reversibility and reducing the degradation typically seen in pristine V_2O_5 systems.

To further quantify the valence state changes of vanadium during the first discharge and charge process, linear combination modeling (LCM) analysis[31] was conducted on the *in operando* XANES spectra, and the results are displayed in Fig. 4f and h. For pristine V_2O_5@G, the initial vanadium valence was found to be approximately 71% V^{5+}, 14% V^{4+}, and 15% V^{3+}, with an

average valence state of 4.5. During the discharge process, the portion of V^{5+} gradually decreases while the V^{3+} and V^{4+} fraction increases simultaneously. Notably, the V^{4+} content remained relatively unchanged after discharging to 50% SOC, suggesting that the reduction of vanadium during lithiation primarily involves transitions between V^{5+} and V^{3+} states, *i.e.* $V^{5+} + 2e^- \rightarrow V^{3+}$. Upon charging, a partial recovery of V^{5+} was observed, but approximately 40% of vanadium remained constantly in the V^{4+} state. This incomplete return to the initial oxidation state suggests that the structure of V_2O_5@G does not fully recover, contributing to the loss of capacity over extended cycling. In contrast, Si-V_2O_5@G exhibits a remarkably different valence evolution profile (Fig. 4h). Initially, the vanadium was composed of 76% V^{5+} and 24% V^{3+}, with no detectable V^{4+} and an average valence of 4.5. During the early stages of discharge (down to 80% SOC), the V^{5+} fraction decreases primarily through conversion to V^{3+}, with no significant V^{4+} formation. From 80% to 20% SOC, V^{5+} (green line) transitioned into both V^{4+} (red line) and V^{3+} (blue line), with V^{4+} increasing more rapidly than V^{3+}. As the SOC approached 10%, V^{5+} nearly disappears, and the portion of V^{4+} begins to decline while V^{3+} continues to increase. This evolution indicates a multistep redox mechanism in which vanadium transitions from $V^{5+} \rightarrow V^{3+} \rightarrow V^{4+}$ and then to V^{3+} again as lithiation progresses. Notably, during the subsequent charging process, the valence state transitions are nearly symmetric to those observed during discharge, with V^{3+} converting back to V^{4+} and V^{5+} in reversed order. This symmetry suggests a highly reversible redox mechanism in Si-V_2O_5@G, highlighting its structural and electrochemical robustness.

In summary, the *in operando* XANES and EXAFS results, supported by LCM analysis, clearly demonstrate that Si doping significantly improves the structural stability and electrochemical reversibility of V_2O_5 during the (de)lithiation process. The undoped V_2O_5@G electrode undergoes more severe electronic structure changes and exhibits irreversible valence shifts, indicative of structural degradation. In contrast, Si-doped V_2O_5@G maintains a more stable and reversible electronic structure, as reflected in symmetric spectral features, moderate valence fluctuations, and recoverable local environments. These findings strongly support the conclusion that Si doping enhances both the structural stability and performance of V_2O_5-based cathodes, offering a promising pathway for developing high-energy density and long-life lithium-ion batteries.

4 Conclusions

We developed a method to dope silicon (Si) uniformly into the V_2O_5 framework, integrated with graphene sheets through a sol–gel process to form a 3D nanostructured composite. The optimized Si-doped V_2O_5/graphene nanocomposite (Si-V_2O_5@G) with 10 wt% Si and 2 wt% graphene exhibits exceptionally stable electrochemical performance, delivering a specific capacity of 392 mA h g^{-1} and extraordinary cycling stability with capacity retention of 80% after 589 cycles, which shows significantly better stability than pristine V_2O_5@G. Cyclic voltammetry (CV) and electrochemical impedance spectroscopy (EIS) analysis demonstrate that Si doping improves conductivity and stabilizes the V_2O_5 structure. The XRD analysis exhibits that both V_2O_5@G and Si-V_2O_5@G are in a non-crystalline (amorphous) structure when integrated with the graphene matrix. XPS results demonstrate that Si doping effectively tailors the electronic structure of V_2O_5 by inducing partial vanadium reduction and strengthening interfacial bonding. Furthermore, *in operando* XANES and EXAFS analyses reveal that Si doping significantly enhances the structural stability and electrochemical reversibility of V_2O_5 during the (de)lithiation process. While pristine V_2O_5@G exhibits asymmetric energy shifts and incomplete valence recovery—indicating poor reversibility, Si-V_2O_5@G shows symmetric spectral evolution and consistent V valence transitions. These results demonstrate that Si incorporation not only stabilizes the V–O framework but also promotes more complete Li-ion extraction and insertion, ultimately leading to improved cycling performance. The findings highlight the effectiveness of Si doping in optimizing the electrochemical behavior of V_2O_5-based cathodes.

Author contributions

Guangqi Zhu: conceptualization, data curation, *in operando* XAS data analysis, investigation, mechanism validation, and writing – original draft. Yadong Liu: conceptualization, material synthesis, electrochemical testing and *in operando* XAS experiment. Yikang Yu, Mohammad Behzadnia, Qi Zhang and Yi-Kai Lien: material synthesis, SEM analysis and writing. Chengjun Sun: *in operando* XAS experiment. Yuzi Liu: TEM analysis. Wenquan Lu and Mangilal Agarwal: materials analysis. Jian Xie: designed the project, manuscript writing, conceived the mechanism, funding acquisition, and supervision.

Conflicts of interest

There are no conflicts to declare.

Data availability

All the data supporting this article have been included in the supplementary information (SI). Supplementary information: Fig. S1 and S2, Table S1 and further experimental details. See DOI: https://doi.org/10.1039/d5ta06057e.

Acknowledgements

This research used resources of Center for Nanoscale Materials and Advanced Photon Source, both Office of Science User Facilities operated for the U.S. Department of Energy (DOE) Office of Science by Argonne National Laboratory, and was supported by the U.S. DOE under Contract No. DE-AC02-06CH11357, and the Canadian Light Source and its funding partners.

References

1 M. S. Whittingham, *Chem. Rev.*, 2004, **104**, 4271–4301.

2 Y. Wang, K. Takahashi, K. H. Lee and G. Z. Cao, *Adv. Funct. Mater.,*, 2006, **16**, 1133–1144.
3 Y. J. Mai, X. L. Wang, J. Y. Xiang, Y. Q. Qiao, D. Zhang, C. D. Gu and J. P. Tu, *Electrochim. Acta*, 2011, **56**, 2306–2311.
4 Y. Tang, X. Rui, Y. Zhang, T. M. Lim, Z. Dong, H. H. Hng, X. Chen, Q. Yan and Z. Chen, *J. Mater. Chem. A*, 2013, **1**, 82–88.
5 J. Wang, N. Yang, H. Tang, Z. Dong, Q. Jin, M. Yang, D. Kisailus, H. Zhao, Z. Tang and D. Wang, *Angew. Chem., Int. Ed. Engl.*, 2013, **52**, 6417–6420.
6 Y. Liu, Q. Liu, Z. Li, Y. Ren, J. Xie, H. He and F. Xu, *J. Electrochem. Soc.*, 2014, **161**, A620–A632.
7 Y. Lu, H. Andersen, R. Wu, A. M. Ganose, B. Wen, A. Pujari, T. Wang, J. Borowiec, I. P. Parkin, M. De Volder and B. D. Boruah, *Small*, 2024, **20**, e2308869.
8 B. D. Boruah, B. Wen and M. De Volder, *Nano Lett.*, 2021, **21**, 3527–3532.
9 A. Chen, C. Li, C. Zhang, W. Li and Q. Yang, *J. Solid State Electrochem.*, 2022, **26**, 729–738.
10 S. A. Hevia, J. Orive, F. Guzmán, E. Cisternas, F. Dietrich, R. Villarroel and J. Lisoni, *Appl. Surf. Sci.*, 2022, **576**, 151710.
11 X. Li, Y. Su, X. Lang, L. Li, C. Yao and K. Cai, *Ionics*, 2022, **28**, 1511–1521.
12 X. Niu, N. Li, Y. Chen, J. Zhang, Y. Yang, L. Tan, J. Wu, L. Guo and Y. Zhu, *Batter. Supercaps*, 2023, **6**, e202300238.
13 F. Coustier, *Solid State Ionics*, 1997, **100**, 247–258.
14 F. Leroux, G. Goward, W. P. Power and L. F. Nazar, *J. Electrochem. Soc.*, 2019, **144**, 3886–3895.
15 F. Coustier, G. Jarero, S. Passerini and W. H. Smyrl, *J. Power Sources*, 1999, **83**, 9–14.
16 M. Lira-Cantú and P. Gómez-Romero, *J. Electrochem. Soc.*, 2019, **146**, 2029–2033.
17 H. Liu and W. Yang, *Energy Environ. Sci.*, 2011, **4**, 4000–4008.
18 X. Ping, X. Pei, D. Zou, C. Wang, X. Li, C. Cao, H. Lei, C. Yang, Q. Cheng, W. Liu, X. Cao, M. Liu and Y. Wang, *Electrochim. Acta*, 2025, **530**, 146297.
19 Y. Zhang, Z. Zou, J. Liu, S. Zhang and H. Zhang, *Mater. Technol.*, 2020, **35**, 887–895.
20 P. Chen, G. Zheng, G. Guo, Z. Wang, J. Tang, S. Li, Z. Wen, S. Ji and J. Sun, *J. Alloys Compd.*, 2019, **784**, 574–583.
21 K. Feng, Y. Li, C. Xu, M. Zhang, X. Yang, Y. Cheng, Y. Wang, L. Yang and S. Yin, *Electrochim. Acta*, 2023, **444**, 142022.
22 T. Partheeban, T. Kesavan, M. Vivekanantha and M. Sasidharan, *Appl. Surf. Sci.*, 2019, **493**, 1106–1114.
23 D. B. Le, S. Passerini, A. L. Tipton, B. B. Owens and W. H. Smyrl, *J. Electrochem. Soc.*, 2019, **142**, L102–L103.
24 A. L. Tipton, S. Passerini, B. B. Owens and W. H. Smyrl, *J. Electrochem. Soc.*, 2019, **143**, 3473–3477.
25 P. Juntree, S. Siriroj, J. Padchasri, P. Songsiriritthigul and P. Kidkhunthod, *J. Alloys Compd.*, 2025, **1016**, 178961.
26 M. Wilhelm, R. Adam, A. Bhardwaj, I. Neumann, S. H. Cho, Y. Yamada, T. Sekino, J. Tao, Z. Hong, T. Fischer and S. Mathur, *Adv. Eng. Mater.*, 2022, **25**, 2200765.
27 Z. Shi, L. Wang, Y. Huang, X. Y. Kong and L. Ye, *Mater. Chem. Front.*, 2024, **8**, 179–191.
28 Y. Yu, G. Zhu, Q. Zhang, M. Behzadnia, Z. Yang, Y. Liu and J. Xie, *ACS Appl. Energy Mater.*, 2024, **7**, 11031–11037.
29 S. Liu, Z. Ding, T. Jiang, T. Chi, H. San, J. Cui, S. Liu, X. Li, X. Li and L. Zhang, *J. Energy Storage*, 2024, **84**, 110822.
30 N. Aliahmad, P. K. Biswas, H. Dalir and M. Agarwal, *Energies*, 2022, **15**, 552.
31 Q. Liu, Z. F. Li, Y. Liu, H. Zhang, Y. Ren, C. J. Sun, W. Lu, Y. Zhou, L. Stanciu, E. A. Stach and J. Xie, *Nat. Commun.*, 2015, **6**, 6127.
32 Q. Liu, Y. Liu, C.-J. Sun, Z.-f. Li, Y. Ren, W. Lu, E. A. Stach and J. Xie, *Electrochim. Acta*, 2014, **136**, 318–322.
33 B. Wang, Y. Wang, B. Sun, P. Munroe and G. Wang, *RSC Adv.*, 2013, **3**, 5069–5075.
34 K. Omosako, T. Watanabe, S. Ogawa and I. Kanno, *Sci. Rep.*, 2025, **15**, 14477.
35 J. Wong, F. W. Lytle, R. P. Messmer and D. H. Maylotte, *Phys. Rev. B*, 1984, **30**, 5596–5610.
36 C. Y. Lee, A. C. Marschilok, A. Subramanian, K. J. Takeuchi and E. S. Takeuchi, *Phys. Chem. Chem. Phys.*, 2011, **13**, 18047–18054.
37 X. Lai, J. E. Halpert and D. Wang, *Energy Environ. Sci.*, 2012, **5**, 5604–5618.
38 F. Xu, H. Zhang, J. Ilavsky, L. Stanciu, D. Ho, M. J. Justice, H. I. Petrache and J. Xie, *Langmuir*, 2010, **26**, 19199–19208.
39 Y. Qian, A. Vu, W. Smyrl and A. Stein, *J. Electrochem. Soc.*, 2012, **159**, A1135–A1140.
40 M. X. Wang, Q. Liu, Z. F. Li, H. F. Sun, E. A. Stach and J. Xie, *J. Phys. Chem. Lett.*, 2013, **4**, 1484–1488.
41 Z. F. Li, H. Zhang, Q. Liu, L. Sun, L. Stanciu and J. Xie, *ACS Appl. Mater. Interfaces*, 2013, **5**, 2685–2691.
42 Y. Liu, Y. Yu, F. Yang, G. Zhu, K. Yu, R. Kou, C. Sun, Y. Liu, J. Xu, C. Liu, C. Li, T. Liu, Y. Ren, W. Lu, R. Ferreira, P. Ferreira, Z. Zhang and J. Xie, *Small*, 2023, **19**, e2206947.
43 J. Livage, *Coord. Chem. Rev.*, 1998, **178–180**, 999–1018.
44 S. Wang, Z. Lu, D. Wang, C. Li, C. Chen and Y. Yin, *J. Mater. Chem.*, 2011, **21**, 6365–6369.
45 M. G. Kanatzidis and S. P. Huang, *J. Am. Chem. Soc.*, 2002, **111**, 760–761.
46 J. Livage, *Chem. Mater.*, 2002, **3**, 578–593.
47 J. Cocciantelli, *Solid State Ionics*, 1995, **78**, 143–150.
48 S. Passerini, *Solid State Ionics*, 1996, **90**, 5–14.
49 M. Giorgetti, S. Passerini, W. H. Smyrl, S. Mukerjee, X. Q. Yang and J. McBreen, *J. Electrochem. Soc.*, 2019, **146**, 2387–2392.
50 A. N. Mansour, P. H. Smith, W. M. Baker, M. Balasubramanian and J. McBreen, *Electrochim. Acta*, 2002, **47**, 3151–3161.
51 E. Almeida, *Solid State Ionics*, 2003, **160**, 61–67.
52 A. M. Cao, J. S. Hu, H. P. Liang and L. J. Wan, *Angew. Chem., Int. Ed. Engl.*, 2005, **44**, 4391–4395.

